Diversity of Mn oxides produced by Mn(II)-oxidizing fungi

Cara M. Santelli [a,1], Samuel M. Webb [b], Alice C. Dohnalkova [c], Colleen M. Hansel [a,*]

[a] Harvard School of Engineering and Applied Sciences, Cambridge, MA, USA
[b] Stanford Synchrotron Radiation Lightsource, Menlo Park, CA, USA
[c] Environmental Molecular Sciences Laboratory, Pacific Northwest National Laboratory, Richland, WA, USA

Abstract

Manganese (Mn) oxides are environmentally abundant, highly reactive mineral phases that mediate the biogeochemical cycling of nutrients, contaminants, carbon, and numerous other elements. Despite the belief that microorganisms (specifically bacteria and fungi) are responsible for the majority of Mn oxide formation in the environment, the impact of microbial species, physiology, and growth stage on Mn oxide formation is largely unresolved. Here, we couple microscopic and spectroscopic techniques to characterize the Mn oxides produced by four different species of Mn(II)-oxidizing Ascomycete fungi (*Plectosphaerella cucumerina* strain DS2psM2a2, *Pyrenochaeta* sp. DS3sAY3a, *Stagonospora* sp. SRC1lsM3a, and *Acremonium strictum* strain DS1bioAY4a) isolated from acid mine drainage treatment systems in central Pennsylvania. The site of Mn oxide formation varies greatly among the fungi, including deposition on hyphal surfaces, at the base of reproductive structures (e.g., fruiting bodies), and on envisaged extracellular polymers adjacent to the cell. The primary product of Mn(II) oxidation for all species growing under the same chemical and physical conditions is a nanoparticulate, poorly-crystalline hexagonal birnessite-like phase resembling synthetic δ-MnO$_2$. The phylogeny and growth conditions (planktonic versus surface-attached) of the fungi, however, impact the conversion of the initial phyllomanganate to more ordered phases, such as todorokite (*A. strictum* strain DS1bioAY4a) and triclinic birnessite (*Stagonospora* sp. SRC1lsM3a). Our findings reveal that the species of Mn(II)-oxidizing fungi impacts the size, morphology, and structure of Mn biooxides, which will likely translate to large differences in the reactivity of the Mn oxide phases.
© 2011 Elsevier Ltd. All rights reserved.

1. INTRODUCTION

Manganese (Mn) oxide and hydroxide minerals, referred to hereinafter as Mn oxides, are ubiquitous in aquatic and terrestrial environments and their presence can have broad environmental ramifications, greatly impacting the fate and transport of organic and inorganic contaminants, nutrients, and carbon sources. For example, Mn(III/IV) oxides act as strong oxidants, capable of degrading recalcitrant or contaminant organic compounds (Forrez et al., 2010; Sunda and Kieber, 1994) and oxidizing redox-sensitive metals such as Cr^{3+} (Fendorf and Zasoski, 1992; Murray et al., 2005; Murray and Tebo, 2007). These highly reactive mineral phases also contribute to sorption and redox reactions of numerous metals, effectively remediating contaminated waters by scavenging metals such as Pb (Matocha et al., 2001; Nelson et al., 1999; O'Reilly and Hochella, 2003; Villalobos et al., 2005), Ni (Kay et al., 2001; Peña et al., 2010), Co (Kay et al., 2001; Takahashi et al., 2007), and Zn (Boonfueng et al., 2009; Marcus et al., 2004; Toner et al., 2006). The oxidizing and sorption capacity of Mn oxide phases, however, is highly dependent upon their size, composition, and structure.

The precipitation of Mn oxide minerals in nature is believed to be largely driven by microbiological activity. Mn(II)-oxidizing bacteria and fungi have been isolated

---

* Corresponding author. Address: Harvard School of Engineering and Applied Sciences, 29 Oxford St., Cambridge, MA 02138, USA. Fax: +1 617 496 1471.
   E-mail address: hansel@seas.harvard.edu (C.M. Hansel).
[1] Present address: Smithsonian Institution, National Museum of Natural History, Department of Mineral Sciences, 10th and Constitution Ave., Washington, DC 20560, USA.

from a wide variety of environments (Adams and Ghiorse, 1987; Cahyani et al., 2009; de la Torre and Gomez-Alarcon, 1994; Dick et al., 2006; Hansel and Francis, 2006; Krumbein and Jens, 1981; Miyata et al., 2006a; Templeton et al., 2005) and can greatly accelerate oxidation rates relative to abiotic processes (Nealson et al., 1988; Tebo et al., 1997). In general, biogenic Mn oxides have greater reactivities relative to abiotic and synthetic analogs, theoretically due to their smaller crystallite size, increased surface area and disorder, and/or sheet symmetry distortion (Hochella et al., 2008; Nelson et al., 1999; O'Reilly and Hochella, 2003).

Over 30 different natural and synthetic Mn oxide minerals are known to exist, largely due to the combination of varied valence states of Mn (Mn can occur in the +2, +3, or +4 oxidation states) and the diverse arrangements of MnO_6 octahedra (the building blocks of Mn oxide structures – Post, 1998). Most Mn oxides are categorized as having either a layer or tunnel structure. Phyllomanganates (layer-structure oxides), such as those within the group of birnessite-like oxides, are composed of stacked sheets of edge-sharing Mn octahedra, whereas tectomanganates (tunnel-structure oxides) have chains of edge-sharing octahedra that are linked through corner-sharing to form square or rectangular cross-sections (e.g., todorokite has a 3×3 tunnel structure). A wide variety of cations can be incorporated into the interlayers and tunnels or adsorbed to the mineral surfaces depending largely on physical properties, such as the atomic structure, crystal morphology, and mineral size (Hochella et al., 2008). Despite the large diversity in Mn oxide structures, the dominant biogenic Mn oxide formed under circumneutral pH is a nanocrystalline phyllomanganate similar to hexagonal birnessite or δ-MnO_2, the synthetic analog of vernadite (Bargar et al., 2005; Jurgensen et al., 2004; Nelson et al., 1999; Villalobos et al., 2006; Webb et al., 2005a). Abiotic transformations and ageing of these initial disordered biogenic phases results in the formation of more crystalline Mn phases, including todorokite and feitknechtite (Bargar et al., 2005; Feng et al., 2010). Oxidation at temperatures ranging from 3 to 70 °C at circumneutral pH results in a wider range of Mn oxides, varying in structure and average oxidation state, which correspond well with the thermodynamic stability fields for these phases (Mandernack et al., 1995).

The majority of studies have thus far characterized Mn oxide phases formed by bacteria, yet in some surface and terrestrial environments, fungal Mn(II) oxidation may be equally or more important than bacterial oxidation (Mariner et al., 2008; Santelli et al., 2010; Thompson et al., 2005). A small number of studies have identified hexagonal birnessite and todorokite as products of fungal Mn(II) oxidation (Miyata et al., 2006a,b; Saratovsky et al., 2009; Grangeon et al., 2010), yet the impact of fungal species, growth conditions, and cellular structures on the properties of fungal Mn oxides have not been investigated. To expand our knowledge of environmentally-relevant biogenic Mn oxides, we examined the Mn oxides precipitated by four phylogenetically and morphologically distinct Mn(II)-oxidizing Ascomycete fungi. These species were recently isolated from biologically-active remediation systems that are currently treating acidic, metal-laden mine waste from abandoned coal mines in Central Pennsylvania (Santelli et al., 2010). We coupled light and electron microscopy techniques with X-ray absorption spectroscopy (XAS) to provide a detailed examination of the fungal oxide phases with respect to fungal species, cellular location (e.g., associated with hyphae, spores, or fruiting bodies), and growth conditions (either water-submerged or on a solid substrate). The results of this study not only provide a better understanding of the products of fungal Mn(II) oxidation, but further elucidate the impact of species diversity on the biogeochemical cycle of metals in the environment.

2. METHODS

2.1. Production of fungal Mn oxides

A diversity of fungal species were obtained from several different passive remediation systems in Central Pennsylvania that actively attenuate high concentrations of Mn within acidic coal mine drainage as described previously (Santelli et al., 2010). Briefly, these treatment systems are geotextile-lined beds filled with limestone rocks, which brings up the pH of the metal-laden waters to near neutral conditions. Under these conditions, the oxidation of dissolved Mn(II) proceeds, resulting in the precipitation of Mn oxide minerals. Mn oxides are retained within the treatment system, and waters flow out with a significantly reduced metal load at near-neutral pH. Four species of Mn(II)-oxidizing fungi (Table 1), representing three different orders of Ascomycota, were explored in this study, including *Plectosphaerella cucumerina* strain DS2psM2a2, *Pyrenochaeta* sp. DS3sAY3a, *Stagonospora* sp. SRC1lsM3a, and *Acremonium strictum* strain DS1bio-AY4a. Cultures for all experiments were inoculated in a HEPES-buffered (20 mM; pH 7) AY medium consisting of 0.25 g L^{-1} sodium acetate, 0.15 g L^{-1} yeast extract, 1 mL L^{-1} trace elements stock (10 mg L^{-1} $CuSO_4 \cdot 5H_2O$, 44 mg L^{-1} $ZnSO_4 \cdot 7H_2O$, 20 mg L^{-1} $CoCl_2 \cdot 6H_2O$, 13 mg L^{-1} $Na_2MoO_4 \cdot 2H_2O$) supplemented with 200 μM $MnCl_2$. The pH and Mn concentrations within AMD treatment systems vary depending of the season, underlying bedrock, influent water chemistry, and the location within the treatment bed. The conditions selected for this study were chosen both to simulate the average measured geochemical conditions (pH 7, 200 μM Mn^{2+}) within several of the treatment systems during a sampling expedition and to compare our study with several other studies examining microbially-induced Mn(II) oxidation.

Since water levels fluctuate dramatically in these open treatment systems, cultures were grown in both a liquid medium (to simulate a submerged environment) or on a solid medium to simulate low water level conditions. For liquid growth experiments, cultures were grown in 50 mL of liquid AY media without agitation because growth is inhibited under stirred conditions. For solid growth experiments, stab cultures were first initiated in petri dishes containing agar-solidified (2% agar) AY media. After growth proceeded radially outwards from the inoculation point, the fungal mycelia were sampled with a sterile coring device

Table 1
List of fungal species with growth conditions and Mn(II) oxidation occurrence.

Sample[a]	Species name	Growth	Location of Mn(II) oxidation
A	*Plectosphaerella cucumerina* DS2psM2a2	Liquid	Hyphae
B	*Plectosphaerella cucumerina* DS2psM2a2	Filter	Hyphae
C	*Pyrenochaeta* sp. DS3sAY3a	Liquid	Hyphae, base of fruiting bodies
D	*Pyrenochaeta* sp. DS3sAY3a	Filter	Hyphae, base of fruiting bodies
E	*Stagonospora* sp. SRC1lsM3a	Liquid	Extracellular
F	*Stagonospora* sp. SRC1lsM3a	Filter	Extracellular
G	*Acremonium strictum* DS1bioAY4a	Liquid	Swollen hyphae
H	*Acremonium strictum* DS1bioAY4a	Filter	Extracellular

[a] Sample designation for XANES, EXAFS, and XRD analysis in Figs. 3–6.

(about 8 mm diameter). The mycelia-containing agar plugs were positioned on cellulose acetate membrane filters (0.2 μm pore size, 47 cm diameter) that had been placed directly on agar-solidified AY media. The filters provided a solid support for the cultures to grow and also allowed diffusion of water-soluble nutrients and metals through the filter, as Mn(II) oxidation was observed on the top surface of the filter. All cultures were incubated in the dark at room temperature for approximately 20–24 days and stored in dark conditions (at −20 °C if long term storage was necessary) until analysis to prevent photoreduction of the Mn oxides (Sunda and Huntsman, 1994). Since some fungal species grow more slowly than others, incubation for 20–24 days ensured sufficient growth of all the fungi on the polycarbonate filters (diameter of all species reached the end of the filter).

2.2. Microscopy

For light microscopy, stab cultures were initiated in agar-solidified AY media supplemented with 200 μM MnCl$_2$ and grown for approximately 2–3 weeks. Radially growing cultures were imaged using a SZX16 Zoom Stereo Microscope (Olympus America Inc.) fitted with an Olympus DP72 Microscope Digital Camera. For electron microscopy, cultures were grown in either liquid media or on filter-supported media supplemented with 200 μM MnCl$_2$. Cultures were grown for approximately 20–24 days, fixed in 2.5% glutaraldehyde, washed 3 times in PBS buffer, and subjected to an ethanol dehydration series. For scanning electron microscopy (SEM), desiccated samples were mounted on double-sided carbon tape and sputter-coated with a Pt/Pd film prior to imaging. SEM was performed at the Harvard University Center for Nanoscale Systems using a Zeiss FESEM Ultra55 with a high efficiency in-lens secondary electron detector. For transmission electron microscopy (TEM), dehydrated cultures were embedded in LR White resin and cured at 60 °C overnight. Hardened resin blocks were sectioned to 70 nm with a Diatome 45° diamond knife using a Leica UCT ultramicrotome (Leica Microsystems) and mounted on 100 mesh copper grids with formvar support film coated with carbon. Unstained sections were imaged with an FEI Tecnai T-12 cryo-TEM. Thin sections for *Plectosphaerella* sp. and *Acremonium* sp. were examined using a JEOL 2010 high resolution TEM (HR-TEM) equipped with an Oxford ISIS Energy-dispersive X-ray spectroscopy (EDS) microanalysis system.

2.3. X-ray absorption spectroscopy (XAS)

Fungi with associated Mn oxides growing in liquid media were concentrated by centrifugation (∼2000×g) of cultures, decanting the liquid, and rinsing with a series of nanopure water to remove residual MnCl$_2$. Dense cell/oxide pellets were loaded into teflon sample holders for analysis. For filter-grown cultures, the whole filter with attached fungi (including mycelia, spores, fruiting bodies, etc.) was removed from the solid media surface and used directly for analysis. Fungal oxide samples were either analyzed immediately after sampling or frozen at −20 °C (to stop growth and oxidation) and thawed just prior to analysis. Lexan windows were secured on each side of the sample holder with Kapton tape for each sample preparation. Manganese K-edge XAS spectra of fungal Mn oxides were collected at beam line 11-2 at the Stanford Synchrotron Radiation Lightsource (SSRL) using a Si(2 2 0) double-crystal monochromator and harmonic rejection mirror set at a 9 keV cut-off energy. Energy was calibrated using the pre-edge peak of KMnO$_4$ (6543.34 eV). Fluorescence data were collected with a 30-element Ge solid-state detector array with soller slits and Cr X-ray filters. Spectra were collected (3–4 scans per sample) at room temperature from −200 to approximately +1000 eV around the Mn K-edge (6539 keV). Analysis of the near edge region (XANES) of consecutive XAS spectra for each culture (both liquid and filter-supported growth) provided no evidence that the X-rays were reducing Mn(IV) to Mn(II). Earlier analysis with cultures grown directly on/in agar indicated a substantial amount of photoreduction of the Mn oxides due to the high carbon levels in the agar-solidified media. This problem was averted by instead growing the fungi on filters for XAS analysis.

Data analysis of sample spectra was performed using the SIXPACK software program (Webb, 2005). XAS scans were averaged, background-subtracted, normalized, and deglitched if necessary. The composition and structure of the Mn oxides were determined using both X-ray absorption near edge spectroscopy (XANES) and extended X-ray absorption fine structure (EXAFS) spectroscopy. The lineshapes (peak position and peak shape) of the XANES spectra were used to estimate the proportions of Mn(II), Mn(III), and Mn(IV) in biogenic and environmental Mn oxides (Bargar et al., 2005; Villalobos et al., 2003; Webb et al., 2005a,b). For XANES analysis, the normalized absorption spectra were analyzed using a data range of

6560–6600 eV. Linear least-squares combination fitting (LCF) of the individual Mn XANES spectra was performed using a spectral reference library of model Mn compounds to identify and quantify the spectral components. The model compounds used were described previously (Bargar et al., 2005): δ-MnO$_2$, hexagonal Na-birnessite, triclinic Ca-birnessite, groutite (α-MnOOH), feitknechtite (β-MnOOH), manganite (γ-MnOOH), hausmannite (Mn$_3$O$_4$), synthetic todorokite ((Na, Ca, K) (Mg, Mn)Mn$_6$O$_{14}$•5H$_2$0), pyrolusite (β-MnO$_2$), synthetic Mn$_2$O$_3$, aqueous Mn(III) pyrophosphate, aqueous MnCl$_2$, and aqueous MnSO$_4$. Binding energies were fixed and negative component contributions were prohibited for LCF. The goodness of fit was established by the minimization of the R-factor parameter (Newville, 2001).

Manganese K-edge EXAFS analysis provided a detailed structural characterization of biogenic Mn oxide minerals by examining the local coordination environment around Mn (Feng et al., 2010; Saratovsky et al., 2009; Villalobos et al., 2006; Webb et al., 2005a,b). For EXAFS analysis, the $\chi(k)$ spectra were k^3-weighted and analyzed using a k range of 3–12 Å^{-1}. Although data were collected to 15 Å^{-1}, an Fe K-edge was observed in most samples, likely from the yeast extract in the media. For samples with resolvable data beyond $k = 12$ Å^{-1}, we obtained comparable results extending the window of analysis to 15 Å^{-1}. For consistency, here we report the results for all samples using a k range of 3–12 Å^{-1}. Principal component analysis (PCA) was performed on the EXAFS spectra to establish the number of components representing the entire data set (for a description of the application of PCA in XAS analysis see Manceau et al., 2002). Target transformations were conducted using a subset of the Mn model compound reference library to evaluate the fitness of each model compound to the overall data set. Model compounds with SPOIL values <6 were used for subsequent LCF of individual fungal Mn EXAFS spectra. SPOIL is a figure of merit used to determine the degree to which replacing an abstract component with the candidate would increase the fit error (Manceau et al., 2002). The SPOIL value is a dimensionless value, where <1.5 is excellent, 1.5–3 is good, 3–4.5 is fair, 4.5–6 is poor, and >6 is unacceptable (Malinowski, 1978). For LCF, binding energies were not allowed to float, a negative component contribution was prohibited, and components were not summed to 1.0.

Distinguishing between the phyllomanganates is difficult due to the similarities in the oxide structures when they are hydrated, small, and highly disordered. Since many of the Mn–O and Mn–Mn distances are similar between the various phyllomanganate structures, a full multiple scattering model that is sensitive to the bending of the Mn octahedral layer and Mn site vacancies provides diagnostic features to distinguish between the phases. Thus, detailed structural EXAFS fitting of select sample spectra was performed using models for a layered phyllomanganate or todorokite structure as described in detail previously (Webb et al., 2005a). Briefly, the model consists of all single scattering (SS) paths (Mn–O and Mn–Mn paths) and three types of collinear multiple scattering (MS) paths (3 legged Mn–Mn–Mn and 4 legged Mn–Mn–Mn–Mn paths) that are less

than 6 Å from the absorbing Mn atom. The distances and Debye-Waller factors for MS paths are fully parameterized based on the SS paths that define them (Hudson et al., 1996). The amplitude of the MS paths is strongly affected by the level of distortion of the phyllomanganate layers, which is accounted for in the model as an out-of-plane bending angle, β (Ressler et al., 1999; Webb et al., 2005a). Distortion of the layer plane may occur in either or both of the in-plane crystallographic directions. The occupancy of the lattice is characterized by the "f_{occ}" parameter, which accounts for both the vacancies within the phyllomanganate layer as well as edge effects in very small nanoparticulate Mn oxides. These two effects cannot be effectively separated, although their relations have been described in detail in Webb et al. (2005a).

2.4. Synchrotron-based X-ray diffraction (SR-XRD)

SR-XRD was performed on fungal Mn oxide samples using SSRL beamline 11-3 with an incident X-ray energy of 1270.375 eV. XRD patterns were collected on hydrated Mn oxide samples initially used for XAS analysis. For XRD analysis, however, the lexan windows were removed due to high background contributions and the oxide slurry was held in place by scotch tape. The XRD patterns were calibrated with lanthanum hexaboride (LaB$_6$). The open source software program XRD-BS (http://www-ssrl.slac.stanford.edu/~swebb/xrdbs.htm) was used to subtract background interference from the scotch tape and the polycarbonate filter (if necessary). Background-subtracted, two-dimensional XRD patterns were subsequently analyzed using the software program Area Diffraction Machine (http://code.google.com/p/areadiffractionmachine/).

3. RESULTS AND DISCUSSION

3.1. Localization and morphology of fungal Mn oxides

Microscopic investigations of Mn oxide-cellular relationships reveal that the patterns of Mn oxide deposition vary considerably between four different Ascomycete species (listed in Table 1). Fig. 1 (specifically A, C, E, and G) shows four fungal species growing radially outward through hyphal extension from the inoculation point in the center of the petri dishes. The hyphae of these species are colorless (see growing tip of hyphae in Fig. 1A, inset), and the brown/black color is due to the presence of Mn oxide minerals. It is evident that the distribution of Mn oxides precipitated by the fungi varies distinctly depending on the species. For example, Mn oxides precipitated by *P. cucumerina* strain DS2psM2a2 are associated primarily with hyphal surfaces (Fig. 1A and B). Mn(II) oxidation proceeds initially in distinct locations along the cell wall, as evidenced by the spherical oxide deposits, and with time the oxides encrust the length of the hyphae (Fig. 1B). *Pyrenochaeta* sp. DS3sAY3a similarly precipitates Mn oxides along the hyphae (Fig. 1D), yet with a less uniform distribution – broad rings are sporadically (not associated with any obvious physiological responses such as a circadian rhythm) distributed circling the inoculation point in
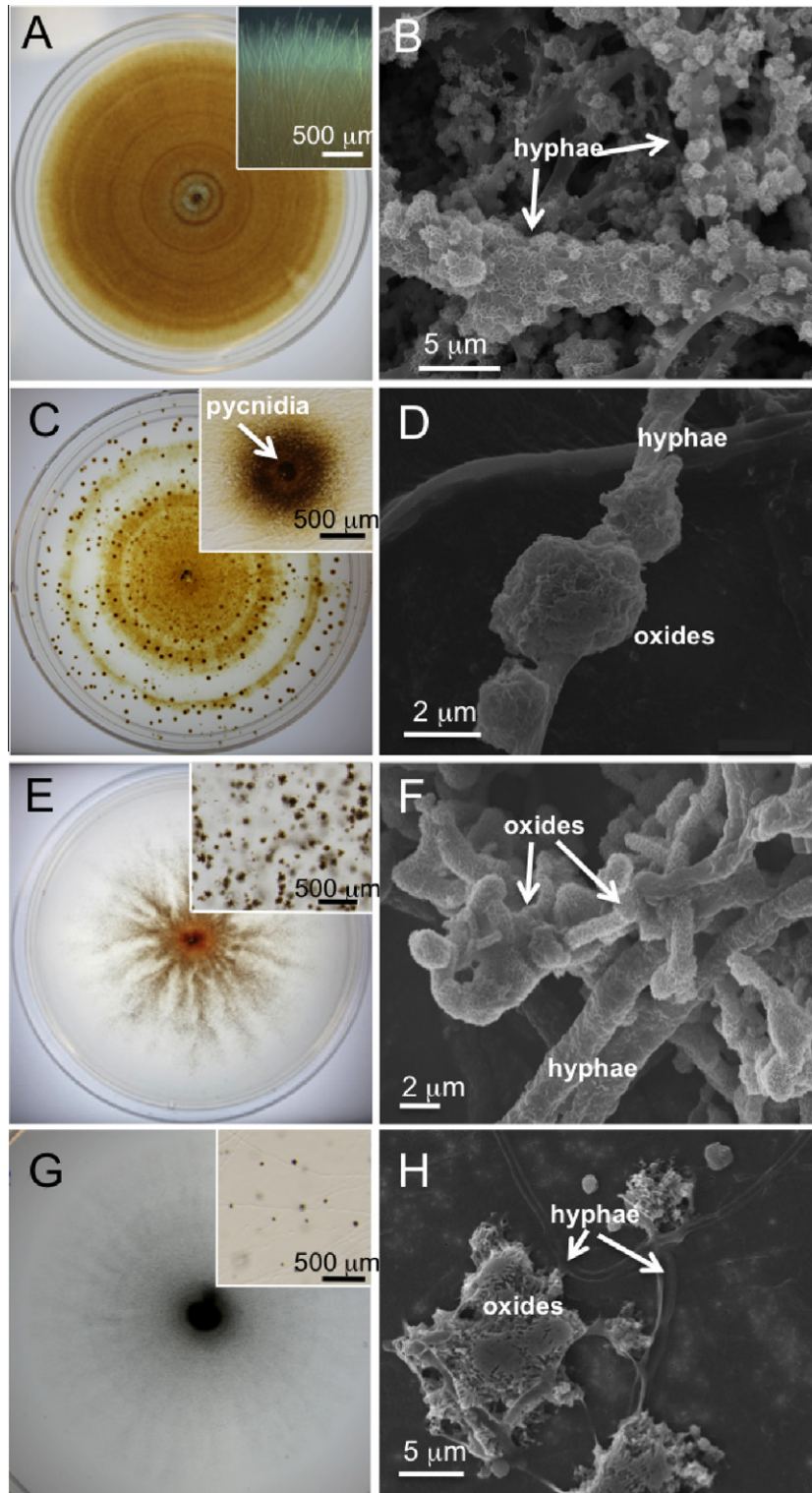
Fig. 1. Micrographs of fungal species *Plectosphaerella cucumerina* DS2psM2a2 (A and B), *Pyrenochaeta* sp. DS3sAY3a (C and D), *Stagonospora* sp. SRC1lsM3a (E and F), and *Acremonium strictum* DS1bioAY4a (G and H) growing in media supplemented with 200 mM Mn^{2+}. Light microscopy (first column), and SEM (2nd column) images show the relationship between mycelium (hyphae) and Mn(III/IV) oxides. The brown/black color in light microscopy images are the result of Mn(III/IV) oxides precipitated by the fungi. Petri dishes are 10 cm in diameter. For SEM images, fungal species were grown in liquid medium with the exception of *Acremonium* sp., which was grown on a filter membrane (solid medium). (For interpretation of the references to colour in this figure legend, the reader is referred to the web version of this article.)

Fig. 1C. Oxide deposition also occurs in association with fruiting body formation (brown oxidation halos around dark spherical pycnidia in Fig. 1C, inset). Mn oxides precipitated by *Stagonospora* sp. SRC1lsM3a, however, are not directly associated with the cell surface but appear as small, dense clusters adjacent to the hyphae (Fig. 1E, inset, 1F). For *Plectosphaerella*, *Pyrenochaeta*, and *Stagonospora* species, the Mn oxide-cellular relationships are similar for isolates grown under planktonic and surface-attached conditions (Table 1). The location of oxides deposited by *A. strictum* strain DS1bioAY4a, however, varies depending on the culture media. Specifically, during growth in liquid media (not shown), oxidation occurs on swollen hyphae, a feature sometimes observed in cultures grown under stressed conditions (e.g., *Penicillium griseofulvum* grown in

low pH media; Bent and Morton, 1963). During growth on solid substrates (both within the agar and on the filter surfaces), however very small, black, blocky clusters of Mn oxides that are not associated with cellular structures (Fig. 1G and H) occur.

The external morphology of the oxides varies between the species (Figs. 1 and 2), likely a consequence of the mechanism and location of oxidation. For example, the Mn oxides produced by *Plectosphaerella* (Figs. 1B and 2A–C) have a typical nanoparticulate, plate-like morphology frequently observed for Mn(II)-oxidizing bacteria (Feng et al., 2010; Toner et al., 2005; Villalobos et al., 2003). These oxides appear to nucleate on the fungal hyphal surfaces, growing radially resulting in surface-associated spherical clusters (Fig. 2B). The Mn oxides produced by
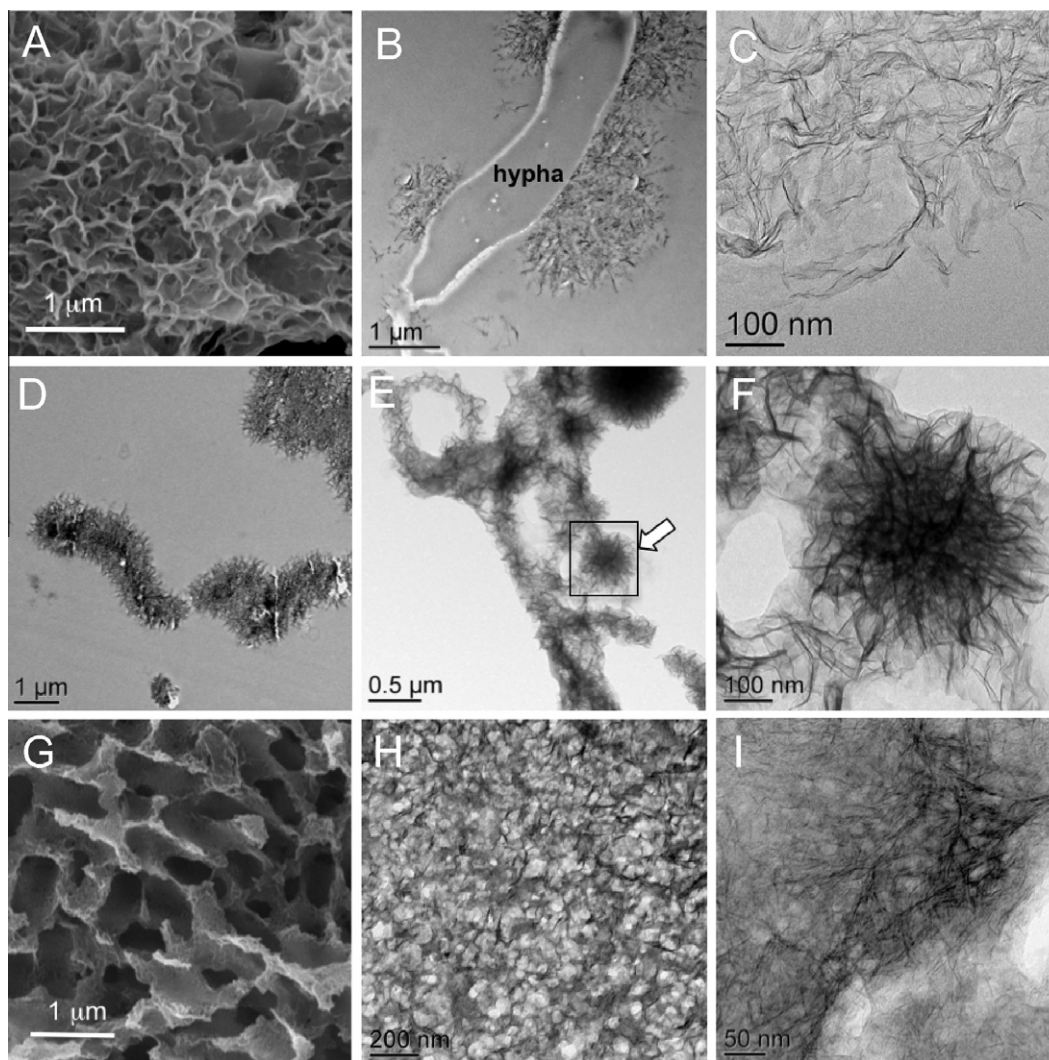

Fig. 2. SEM, TEM, and HR-TEM images of Mn oxides produced by *Plectosphaerella cucumerina* DS2psM2a2 (A–C) *Stagonospora* sp. SRC1lsM3a (D–F), and *Acremonium strictum* DS1bioAY4a (G–I). (A) SEM of thin sheets of Mn oxides on hyphal surface of *P. cucumerina* shown in Fig. 1B. (B) TEM image of a cross-section through the hypha emphasizing the close association of the oxides with the cell surface. (C) HR-TEM image showing the rumpled sheet-like morphology of Mn oxides. (D) TEM image of cross-section through one of the extracellular, thread-like Mn oxide features of Mn oxides produced by *Stagonospora*. (E) TEM image of a whole mount of the thread-like features of Mn oxides. The box highlights area of image (F). (G) SEM image showing a close-up of the extracellular blocks of Mn oxides produced by filter-grown *Acremonium* sp. in Fig. 1H. (H) TEM of cross-section showing a honeycomb-like distribution of oxides that is distinctive from those produced by the other isolates. (I) HR-TEM of densely-packed Mn oxides in (H).

Stagonospora have very small crystal sizes (the lateral dimensions are smaller than those observed for *Plectosphaerella*) that conglomerate in densely-packed threads of crystals (Figs. 1F and 2D–F). Upon closer examination, these oxide masses appear as filaments that are not templated on any visible cellular structures (Fig. 2D). Interestingly, the oxides deposited by surface-grown *A. strictum* strain DS1bioAY4a (Sample H) have more poorly formed sheet morphologies (Fig. 2G) with regions that are thicker and more densely packed, giving the oxide conglomerate a honeycomb-like appearance (Fig. 1H and I). Overall, the Mn oxides are nanoparticulate in nature, having a needle-like or rumpled sheet appearance in cross-section (e.g., Fig. 2B and C, respectively). For all samples, particle sizes range from approximately 2–6 nm in diameter (equivalent to 3–8 layers) and 0.1–1 μm in length. The dimensions of the fungal Mn oxides differ from those typically observed for bacterial Mn oxides. In particular, the fungal Mn oxides are smaller in diameter along the *a* axis (<6 nm v. 10–50 nm) but longer along the *b* axis (up to 1 μm v. <500 nm) than most bacterial Mn oxides (Bargar et al., 2009; Feng et al., 2010; Villalobos et al., 2003). Consistent with our results, however, recent characterization of Mn oxides formed by freshwater fungi found birnessite with average dimensions of 1.5–2.2 nm (2–3 layers) perpendicular to the layer plane (Grangeon et al., 2010). Unfortunately, here attempts to obtain lattice fringes using HR-TEM were unsuccessful because the Mn oxides were highly susceptible to beam damage.

Although the mechanisms and pathways of Mn(II) oxidation are not elucidated for the fungi employed in this study, there are clearly significant differences in the morphology and depositional patterns of Mn oxides between the fungal species suggesting that more than one oxidation pathway is operative. For example, Mn oxides formed directly in contact with hyphal surfaces (*P. cucumerina* and *Pyrenochaeta* sp., Fig. 1B and D) likely involve cell wall associated enzymes. Indeed, a previous study suggests that a laccase-like multicopper oxidase participates in the oxidation of Mn(II) by *A. strictum* strain KR21-2, resulting in Mn(II) oxidation on the hyphal surface (Miyata et al., 2004). Furthermore for the *Pyrenochaeta* and surface-attached *Acremonium* species investigated here, increased deposition of Mn oxides is correlated to the formation of asexual reproductive structures (fruiting bodies) that produce fungal spores (conidia). Localized production of the reactive oxygen species superoxide (O_2^-) has been observed in connection with fruiting body formation in many fungal species (Aguirre et al., 2005) which may lead to oxidation of Mn(II) by superoxide, as we have observed previously for Mn(II) oxidation by some bacteria (Learman et al., 2011). Interestingly, however, the conidia do not directly oxidize Mn(II) (data not shown), unlike many of the previously isolated bacteria which oxidize Mn(II) only in spore form (i.e., several different species of *Bacillus* – Dick et al., 2006; Francis and Tebo, 2002). In contrast, Mn(II) oxidation products formed by the *Stagonospora* species and the surface-attached *Acremonium* species do not appear to be directly associated with any cellular structures (Figs. 1 and 2), as if the oxides are templating on a soluble protein or

metabolite similar to that observed for bacterial Fe(II) oxidation (Chan et al., 2004, 2009). Many fungi produce large quantities (mM levels) of organic acids (e.g., oxalate, citrate) and exopolymers (Gadd, 2007). In fact, the filamentous Mn oxides formed by *Stagonospora* sp. (Figs. 1F and 2D) are morphologically similar to those formed by a Mn(II)-oxidizing Basidiomycete fungus and the Mn(II)- and Fe(II)-oxidizing bacterium *Leptothrix discophora* strain SS-1 (Emerson et al., 1989). These *Metallogenium*-like Mn oxide structures were also found at a distance from the fungal and bacterial cell, and it was suggested that the Mn oxides deposited on a matrix of anionic polymers, likely containing acidic polysaccharides and a Mn(II)-oxidizing protein (Emerson et al., 1989) – similar to the mechanism proposed for Mn oxide encrustations on the surface of budding and sheathed bacteria (Ghiorse, 1984). Templated growth along the hyphal surfaces or exopolymers may also contribute to the elongated growth of the fungal Mn oxides along the *b* axis in contrast to bacterial oxides.

3.2. Composition of fungal Mn oxides

The Mn K-edge XANES spectra for Mn oxides precipitated by the four different species of Ascomycete fungi grown under planktonic (i.e., fully submerged in liquid media) or surface-attached (i.e., on a filter membrane) conditions are shown in Fig. 3A (A–H; solid lines). The energy position of the XANES absorbance maximum for all the fungal Mn oxides centers around 6562 eV. This position is consistent with the absorbance maximum of δ-MnO_2, which has an oxidation state of 3.9–4.0, suggesting that the fungal biooxides are dominated by Mn(IV). Peaking broadening of the absorption maxima (particularly sample H), may reflect a higher contribution from Mn(III). While the average oxidation state is reflective of the predominance of Mn(III)/(IV) within the solids, a contribution of Mn(II) to the XANES spectra is evidenced by a shoulder at 6553 eV in the fungal Mn oxide spectra, with the exception of sample F. The relative contribution of Mn(II) within the fungal biooxides was determined via linear combination fitting (LCF) of the XANES spectra (Fig. 3, dotted lines). LCF of the Mn XANES reveals that all the fungal biooxide spectra can be reconstructed using four Mn components, aqueous Mn(II) (as $MnCl_2$), δ-MnO_2, triclinic Ca-birnessite, and todorokite (only for sample H). Fits were greatly improved (χ^2 was reduced by >80%) by adding aqueous Mn(II) as a component to all spectra (17–27%) except the filter-grown *Stagonospora* sp. SRC1lsM3a (Sample F – Fig. 3b). The coordination of Mn^{2+}, either adsorbed to or incorporated within the oxides or taken up intracellularly by these organisms, is not established in this study. Since the edge shapes of the phyllomanganates (δ-MnO_2, hexagonal and triclinic birnessite) and tectomanganates (todorokite) are similar due to the similarity in the short-range structure of the phases, especially when highly disordered and present as nanoparticulate phases, LCF analysis of the EXAFS spectra was conducted to discern the structure of Mn within the fungal oxides (Fig. 4, Table 2).

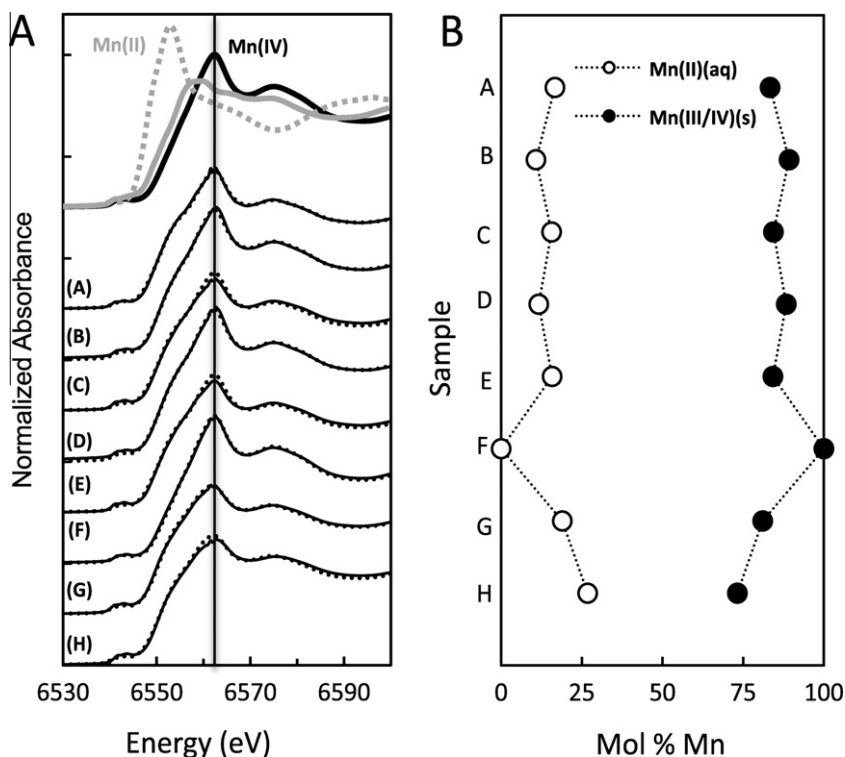Although the morphology and localization of the oxides vary substantially between the fungal species, the

Fig. 3. (A) Mn XANES data for fungal Mn oxides from samples A–H and Mn. Also depicted are the reference compounds aqueous $MnCl_2$ (dashed gray), Mn_2O_3 (solid gray) and δ-MnO_2 (thick black), which emphasize the positions of the white lines (absorption maxima) for Mn(II), Mn(III), and Mn(IV), respectively, at increasingly higher energies. Thin solid lines (A–H) denote the sample data, and fits to data are in dotted lines. The vertical line at 6562 eV indicates the position of the white line for Mn(IV) species. (B) Results of the linear combination fitting (LCF) of the fungal Mn oxides using spectra from numerous Mn-containing model compounds of varying oxidation states, revealing the fraction of Mn(II) associated with the fungal biooxide phases.

composition and structure of the oxides revealed via LCF-EXAFS (Fig. 4) is not distinctly different for most species and growth conditions, with one exception. A disordered, nanoparticulate layered Mn oxide phase resembling hexagonal birnessite or synthetic δ-MnO_2 is the primary phase deposited by the four different Mn(II)-oxidizing Ascomycete species when grown in media with the same solution chemistry (Figs. 4, Table 2). And with the exception of one species, *A. strictum* strain DS1bioAY4a, the Mn oxides deposited by these fungi consist of only layer-structure phases regardless of growth conditions (planktonic or surface-attached). Specifically, inspection of the experimental data reveals similar spectra for all fungal Mn oxides, with subtle differences in the region between 7.5 Å^{-1} and 9.5 Å^{-1}, the "indicator region" (Fig. 4, gray shading) for phyllo- and tecto-manganate structures (McKeown and Post, 2001; Saratovsky et al., 2009; Webb et al., 2005a). Principle component analysis (PCA) reveals that each fungal Mn oxide spectra can be summarized using a maximum of two components (Table 2, Fig. 4 – dashed lines). δ-MnO_2 provides the best (and most significant) fit to the fungal Mn oxide EXAFS data, except for *Stagonospora* sp. SRC1lsM3a (sample F) and *A. strictum* strain DS1bioAY4a grown on a solid substrate (sample H). The *Stagonospora* sp. and *A. strictum* sp. produce Mn oxides that are best fit with a combination of δ-MnO_2 and triclinic Ca-birnessite and δ-MnO_2 and todorokite, respectively. Examination of the spectral fingerprints for these model

compounds (Fig. 4) correspondingly emphasizes the differences in the "indicator" region observed in the experimental data. In particular, the two distinct peaks at 8 Å^{-1} and 9.3 Å^{-1} in the δ-MnO_2 and samples A–G spectra give way to a more broad, gradually-rising slope for the todorokite and sample H spectra – attributed to interference from the 4 different crystallographic sites for Mn in todorokite as opposed to the dominance of a single Mn site in phyllomanganate structures (McKeown and Post, 2001). Similar to the XANES analysis (Fig. 3b), the fits to several of the experimental spectra, particularly samples A–D, were correspondingly improved by small contributions of aqueous Mn(II) (as $MnCl_2$).

Results from numerous studies characterizing the oxidation products deposited by several different species of Mn(II)-oxidizing bacteria have similarly demonstrated that a poorly-crystalline phyllomanganate with hexagonal symmetry (similar to δ-MnO_2) is the primary Mn oxide phase formed under many environmental conditions (Bargar et al., 2005; Jurgensen et al., 2004; Villalobos et al., 2003, 2006; Webb et al., 2005a,b). Furthermore, X-ray diffraction (XRD) and XAS analysis of the Mn oxides deposited by several species of Ascomycete fungi growing under planktonic conditions (Miyata et al., 2006a,b; Grangeon et al., 2010) also identified δ-MnO_2-like mineral phases. Todorokite, however, is a less frequently observed product of microbial Mn(II) oxidation. Webb et al. (2006) demonstrated
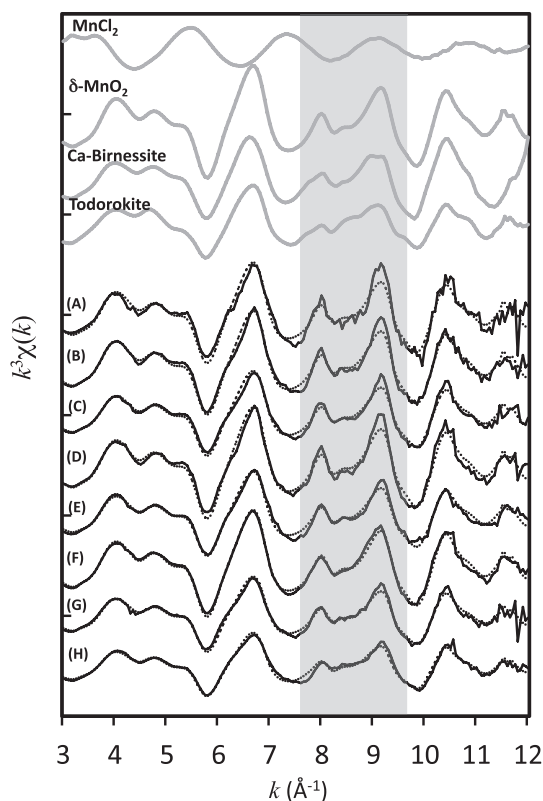
Fig. 4. Mn EXAFS data for fungal Mn oxides from samples A–H and reference compounds used for linear combination fitting (LCF). Data shown in solid lines and fits to data in dotted lines. The gray shaded area highlights the "indicator region" emphasizing the spectral differences between δ-MnO$_2$ and todorokite. Corresponding LCF-EXAFS values are provided in Table 2.

bed in Japan (Miyata et al., 2004; Saratovsky et al., 2009), shares 100% sequence similarity (ITS regions – Santelli et al., 2010) with strain DS1bioAY4a analyzed in this study. Based on the results illustrated here, the differences in the previous *Acremonium* sp. studies may, in fact, be due to growth conditions; studies that observed layered Mn oxides were formed by planktonic cultures (Miyata et al., 2006a,b; Grangeon et al., 2010), while todorokite was identified when fungi were grown on agar surfaces (Petkov et al., 2009; Saratovsky et al., 2009). In contrast to the mixed hexagonal birnessite and todorokite products formed by strain DS1bioAY4a here, however, surface grown KR21-2 produced only todorokite (i.e., phyllomanganates were not detected).

3.3. Structural model of the fungal Mn oxides

To obtain a more detailed structural analysis of the fungal biooxides, we employed a full multiple scattering model that is sensitive to bending of the Mn octahedral layer and Mn site vacancies as described in detail previously (Webb et al., 2005a). The out-of-plane bend (β angles along the a- and b-axes) and Mn layer site vacancies (f_{occ}) are diagnostics for distinguishing between the phyllomanganates and tectomanganate (Fig. 5). Specifically, three representative spectra are selected for a more rigorous Mn EXAFS fitting to obtain quantitative information about fungal Mn oxide structures: (1) a phyllomanganate with measurable Mn(II) – *P. cucumerina* strain DS2psM2a2 grown in liquid media, sample A; (2) a phyllomanganate with negligible Mn(II), exemplified by *Stagonospora* sp. SRC1lsM3a grown in liquid (sample F); and (3) *A. strictum* strain DS1bioAY4a grown on a solid substrate (sample H) with attributes of both a layered and tunnel structure based on LCF analysis of the EXAFS spectra (Fig. 6, Table 3).

As depicted in Fig. 5, the fungal Mn oxides data in k-space (Fig. 6A, solid lines) and R space (Fig. 6B, solid lines) are well reproduced by the EXAFS model (dashed lines). Fitting parameters (Table 3) for *P. cucumerina* (sample A) reveal a Mn oxide structure with negligible out-of-plane bending of the octahedral layers ($\beta_{a-axis} = \beta_{b-axis} = 0$), a high number of corner-sharing Mn octahedra (Mn–Mn corner CN = 2.2), and the fraction of occupied Mn octahedral sites is high ($f_{occ} = 0.91$) as a result of continuous chains of edge-sharing Mn octahedral. These parameters, coupled

that a poorly ordered, tunnel-type mineral structure similar to todorokite can form during Mn(II) oxidation by *Bacillus* sp. SG-1 in the presence of uranyl. Here, *A. strictum* strain DS1bioAY4a produces solely δ-MnO$_2$ when grown planktonically, but both δ-MnO$_2$ and todorokite are observed when grown on a surface (Table 2). Previously, the Mn oxides produced by *A. strictum* strain KR21-2 were identified as solely todorokite (Petkov et al., 2009; Saratovsky et al., 2009) or layered Mn oxides (Grangeon et al., 2010). *A. strictum* strain KR21-2, originally isolated from a stream-

Table 2
Results of linear least-squares fitting analysis for Mn EXAFS spectra of fungal Mn oxides.

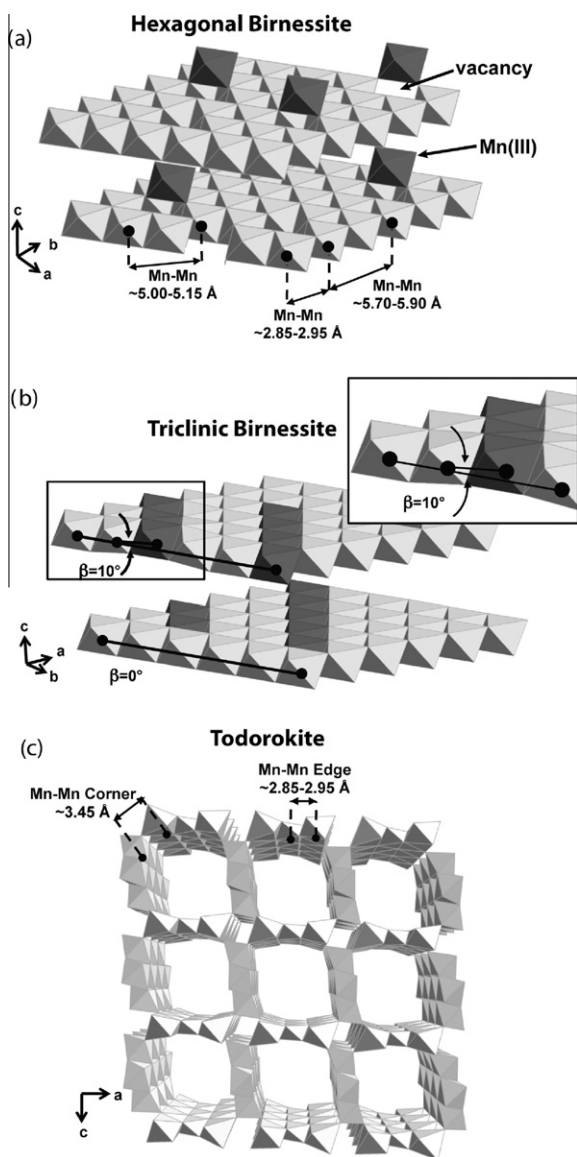| Sample | Fit components | | | | Sum | R-factor | χ^2 |
	MnCl$_2$	δ-MnO$_2$	Todorokite	Tri-birnessite[a]			
A	0.27	0.94	0	0	1.24	0.10	1.84
B	0.15	0.95	0	0	1.10	0.04	0.80
C	0.12	0.77	0	0	0.89	0.05	0.54
D	0.18	1.02	0	0	1.19	0.05	1.05
E	0	0.75	0	0	0.75	0.04	0.47
F	0	0.8	0	0.19	0.99	0.01	0.23
G	0.06	0.68	0	0	0.74	0.06	0.53
H	0	0.45	0.17	0	0.72	0.04	0.29

[a] Triclinic Ca-birnessite.

Fig. 5. Simplified polyhedral representation of the crystal structures of the Mn oxides observed in this study, hexagonal birnessite (a), triclinic/pseudo-orthogonal birnessite (b), and todorokite (c). The dark shaded octahedra in the birnessite structures represent lattice positions of Mn^{3+} octahedra. Interlayer cations are omitted for simplicity. Simplified illustration of the out-of-plane bending angle (β) is depicted for triclinic birnessite (inset).
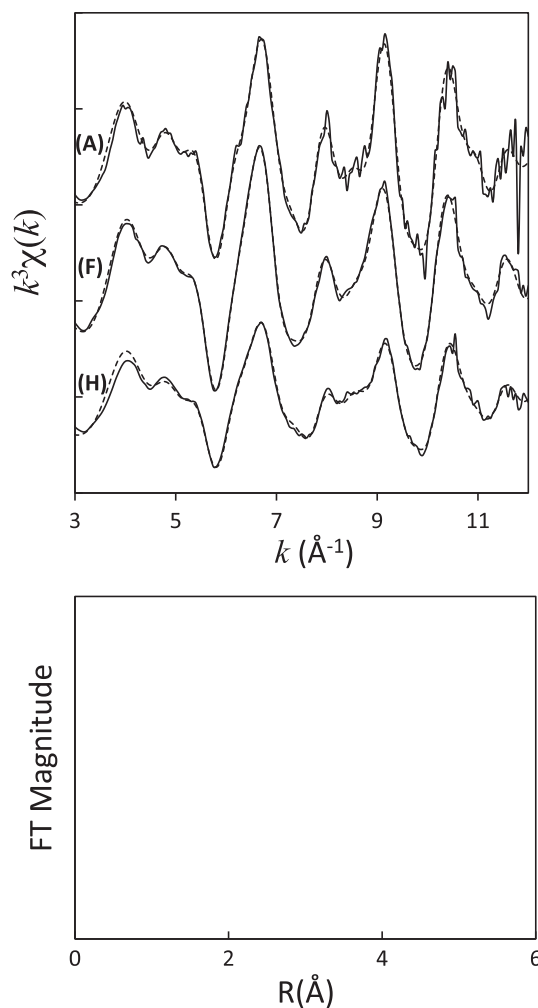

Fig. 6. Mn EXAFS data (solid lines) and the structural EXAFS fitting results (dashed lines) of a few representative fungal Mn oxides (samples A, F, and H) in k^3-space (A) and R-space (B). Corresponding model parameter results are provided in Table 3.

with the EXAFS LCF analysis (Fig. 4, Table 2), suggests that the structure is intermediate between δ-MnO_2 and hexagonal birnessite with fewer vacancies in the Mn octahedral layer than is commonly observed for these phases (Webb et al., 2005a). The local structure of δ-MnO_2 and hexagonal birnessite is similar except for less Mn–Mn corner linkages and a lower degree of sheet stacking order along the c axis (generally limited to 2–3 layers) for the former phase (Lanson et al., 2000; Silvester et al., 1997; Villalobos et al., 2003). The higher Mn–Mn corner coordination observed for *P. cucumerina* biooxides suggests that the structure is most similar to hexagonal birnessite, yet there is a high degree in

uncertainty in determining the coordination numbers of the corner Mn (Webb et al., 2005a). SR-XRD measurements exhibit two broad, asymmetric peaks at 2.45 and 1.43 Å, which originate from the in-layer (2 0 0)/(1 1 0) and (3 1 0)/(0 2 0) birnessite reflections (Fig. 7). Also evident in the XRD data is a broadened basal (0 0 1) peak and absence of a (0 0 2) reflection (Fig. 7), which together with the asymmetry of the ($h\,k\,0$) reflections suggests that the phyllomanganates contain a small number of stacked layers (along the c axis) that are turbostratically disordered (successive layers are rotated and sheared relative to one another) as frequently observed for Mn biooxides (Bargar et al., 2005; Feng et al., 2010; Villalobos et al., 2003; Webb et al., 2005a; Zhu et al., 2010). Thus, the SR-XRD results suggest that the fungal biooxide is more similar to δ-MnO_2 or a c-disordered hexagonal birnessite where the lack of stacking normal to the layers results in the observed lack of long-range structural coherence.

For *Stagonospora* sp. (sample F), the f_{occ} parameter is similar to the *P. cucumerina* biooxides, however the

Table 3
Summary of parameters from Mn K-edge EXAFS fitting of select fungal Mn oxides using the full multiple scattering Mn oxide model developed by Webb et al. (2005a).

Sample	R	χ^2	f_{occ}[a]	f_{dival}[b]	$\beta(a\text{-axis})$[c]	$\beta(b\text{-axis})$[c]	Shell	CN	Dist (Å)	σ^2
A	0.0062	50.3	0.91(9)	0.22(4)	0(5)	0	Mn–O	4	1.86(1)	0.003(1)
							Mn–O	2	1.95(2)	
							Mn–Mn edge	2	2.83(1)	0.005(1)
							Mn–Mn edge	4	2.87(1)	
							Mn–O	4	3.58	0.006(9)
							Mn–O	2	3.67	
							Mn–Mn corner	2.2(1.1)	3.51(4)	0.004(8)
							Mn–interlayer	1.1(0.9)	4.18(9)	0.006(5)
							Mn–O	4	4.4(2)	0.005(4)
							Mn–O	8	4.7(2)	
							Mn–Mn diag	4	4.91(5)	0.004(4)
							Mn–Mn diag	2	5.06(7)	
							Mn–Mn next	2	5.66	0.01(1)
							Mn–Mn next	4	5.74	
							Mn^{2+}–O	6	2.21(2)	0.003
F	0.0044	50.7	0.93(9)	0.15(4)	7(4)	0	Mn–O	4	1.86(1)	0.003(1)
							Mn–O	2	1.95(2)	
							Mn–Mn edge	2	2.82(1)	0.005(1)
							Mn–Mn edge	4	2.89(1)	
							Mn–O	4	3.58	0.007(9)
							Mn–O	2	3.67	
							Mn–Mn corner	1.0(0.8)	3.49(4}	0.004(8)
							Mn–interlayer	0.7(1.0)	4.2(1)	0.006(5)
							Mn–O	4	4.3(4)	0.02(2)
							Mn–O	8	4.8(2)	
							Mn–Mn diag	4	4.93(8)	0.008(7)
							Mn–Mn diag	2	5.1(1)	
							Mn–Mn next	2	5.65	0.01(1)
							Mn–Mn next	4	5.79	
							Mn^{2+}–O	6	2.26(2)	0.003
H	0.0103	69.9	0.56(8)	0.24(4)	2(5)	7(5)	Mn–O	4	1.86(1)	0.003(1)
							Mn–O	2	1.98(2)	
							Mn–Mn edge	2	2.82(3)	0.06(2)
							Mn–Mn edge	4	2.87(2)	
							Mn–O	4	3.58	0.01(1)
							Mn–O	2	3.67	
							Mn–Mn corner	2.9(1.2)	3.46(2)	0.005(6)
							Mn–interlayer	0.3(1.0)	4.0(2)	0.006(5)
							Mn–O	4	4.1(3)	0.02(1)
							Mn–O	8	4.7(2)	
							Mn–Mn diag	4	4.90(8)	0.005(8)
							Mn–Mn diag	2	5.05(9)	
							Mn–Mn next	2	5.64	0.01(1)
							Mn–Mn next	4	5.74	
							Mn^{2+}–O	6	2.21(2)	0.003
Reference spectra[d]:										
δ-MnO$_2$	0.0097	1932	0.77(8)	ND[c]	0(4)	0(4)	Mn–Mn corner	0.6(1.0)	3.43(5)	0.005(4)
Triclinic Birnessite	0.0145	1291	0.90(8)	ND	15(5)	0(5)	Mn–Mn corner	0.8(8)	3.36(9)	0.006(3)
Hexagonal Birnessite	0.0217	1494	0.77(9)	ND	1(5)	0(5)	Mn–Mn corner	2.0(1.1)	3.48(1)	0.003(3)
Todorokite	0.0210	8020	0.604(4)	ND	6(3)	19(3)	Mn–Mn corner	2.9(1.3)	3.46(7)	0.005(0.02)

[a] f_{occ} represents the fraction of occupied Mn octahedra in the mineral structure.
[b] f_{dival} represents the fraction of divalent, Mn^{2+} cations accounted for in the structural model.
[c] The out-of-plane bending angles, β-angles, are measured in degrees.
[d] The fit results for the reference spectra were reported in Webb et al. (2005a).
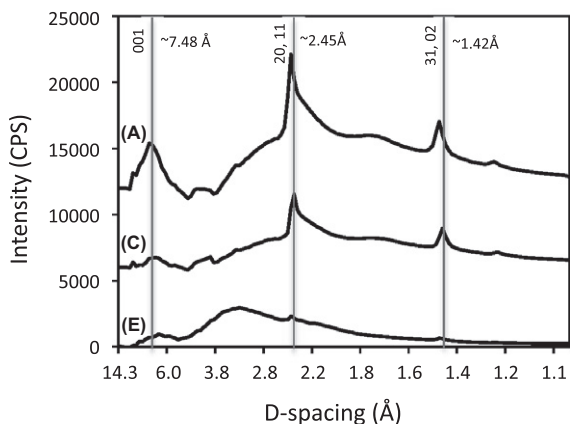[e] Not determined

Fig. 7. X-ray diffraction (XRD) analysis of Mn oxides produced by liquid-grown *Plectosphaerella cucumerina* (sample A), *Pyrenochaeta* sp. (sample C), and *Stagonospora* sp. (sample E). Vertical gray lines emphasize peaks that correspond to those present in synthetic hexagonal birnessite.

coordination number for corner-sharing Mn is lower (1.0) while the bending angle in the *a*-axis increased slightly to a value of 7 (Fig. 6, Table 3). These values fall between the model parameters for hexagonal and triclinic birnessite (Webb et al., 2005a), confirming the LC-EXAFS fits (Fig. 4, Table 2). Triclinic birnessite has pseudo-orthogonal symmetry and is characterized by a large proportion (up to 1/3) of Mn(III) octahedral in the sheets resulting in a charge imbalance that is compensated by hydrated interlayer cations (Lanson et al., 2002; Silvester et al., 1997). If Mn^{3+}-rich rows are formed, lattice strain results in buckling of the planar sheets (Lanson et al., 2002), which is manifested in a large angular non-linearity along one axis (β_A 12–17°) (Webb et al., 2005a). The slight buckling of the octahedral sheets in the biooxides produced by *Stagonospora* suggests that the biooxides contain layer Mn(III) and that either the Mn oxides are transforming from hexagonal to pseudo-orthogonal symmetry or the co-existence of the two phases, possibly at discrete locations. The templated Mn oxides filaments produced by *Stagonospora* (Figs. 1E and F and 2D–F) may in fact consist of a triclinic birnessite core surrounded by hexagonal birnessite. The central polymer may control mineral formation by directing mineral structure and orientation, for instance by reducing the activation energy required for more stables phases, as observed previously for Fe(III) oxide deposition on bacterial polymers (Chan et al., 2004, 2009). Mn(II) oxidation by spores of *Bacillus* sp. strain SG-1 in seawater resulted in two co-existing hexagonal and pseudo-orthogonal birnessite phases with the proportion of the hexagonal phase diminishing over time (Webb et al., 2005a). It was postulated that this transformation was due to the lability of the Mn oxides, especially in the presence of dissolved Mn(II), resulting in the conversion to thermodynamically more stable phases (ie., Ca-pseudo-orthogonal birnessite under seawater conditions) (Webb et al., 2005a). Here, we cannot confirm the presence, association, and abundance of triclinic birnessite within the fungal biooxides. SR-XRD measurements show

only weak, broad, and asymmetric (*h k*) reflections and absence of (0 0 *l*) reflections (Fig. 7), indicative of small, highly disordered phases (Webb et al., 2005a). An indicator of triclinic symmetry is the splitting of the   2.4 and 1.4 Å peaks, yet, the broad, weak (2 0 0, 1 1 0) and (3 1 0, 0 2 0) reflections here preclude this distinction (Fig. 7). Further temporal and spatial investigations are required to determine the relationship and relative significance of the two Mn oxide phases.

In contrast to *P. cucumerina* and *Stagonospora* sp., the fit parameters for *A. strictum* (sample H) show a small degree of bending in both the *a*-axis and *b*-axis and the fraction of Mn octahedra vacancies increase dramatically ($f_{occ} = 0.56$) in concert with the Mn–Mn corner-sharing number (2.9) (Fig. 6, Table 3). The substantially greater degree of vacancies (nearly 45% compared to only   10% for the other spectra), out-of-plane bending, and number of corner sharing Mn octahedra, are indicative of a todorokite component (Webb et al., 2005a). All of these values are intermediates between the hexagonal birnessite and todorokite model compounds (Webb et al., 2005a). The structural analysis corroborates the LCF analysis (Section 3.2 above), where spectral fits to the data were significantly improved by the addition of a todorokite component, and this component contributes approximately 27% of the LC-EXAFS fit (Fig. 4, Table 2). Although the average oxidation state has not been specifically determined for the todorokite reference, most natural todorokites have a significant Mn(III) component, thus the average oxidation state is lower than for δ-MnO$_2$, for example. These results suggest that both layer-structured and tunnel-structured phases are present in the oxides formed by the surface-attached *A. strictum*. Unfortunately, SR-XRD measurements were unsuccessful for any of the fungi grown on solid-substrates, due to the high background produced by the filter. Extensive TEM analysis did not reveal lattice fringes consistent with a tunnel structure suggesting that the todorokite is poorly crystalline with an incoherent tunnel width lacking periodicity in the *c*- and *a*-axis, similar to what has been observed previously for todorokites formed from poorly ordered precursor phyllomanganates (Bodeï et al., 2007; Feng et al., 2010) (see Section 3.4 below). However, in contrast to the predicted poorly-ordered tunnel structure produced by *A. strictum* strain DS1bioAY4a, the todorokite formed by strain KR21-2 (Petkov et al., 2009; Saratovsky et al., 2009) was characterized as oblong plates (some with rectilinear features) with a high degree of crystallinity.

The differences in Mn oxides formed between the two surface grown *A. strictum* strains are likely a consequence of the solution chemistry under which the isolates were growth. Although both isolates were grown on agar-solidified AY medium at room temperature, other conditions varied: pH 6 (strain KR21-2) vs. pH 7 (strain DS1bio-AY4a); inoculation directly within agar-media (strain KR21-2) vs. on a cellulose filter membrane placed above the agar (strain DS1bioAY4a). Also, a significant difference between the two is the Mn concentration of the growth media. The medium for *A. strictum* strain DS1bioAY4a contains 200 μM Mn^{2+} whereas that for strain KR21-2

contains 5 mM Mn^{2+}. Although the mechanisms and pathways of Mn(II) oxidation employed by these two strains could differ, it is likely that pH and particularly Mn(II) concentration are responsible for the dissimilarities in oxidation products and may, in fact, be due to accelerated conversion of hexagonal birnessite to todorokite in the presence of high Mn(II) concentrations (see discussion in Section 3.4 below).

3.4. Implications of hexagonal birnessite and todorokite association

It is plausible that the tunnel-type structures observed by the surface grown *A. strictum* strain DS1bioAY4a are resulting from the conversion of the δ-MnO_2 phase initially precipitated by the fungus. Indeed, this conversion from a layered to tunnel structure has been previously observed in environmental and synthetic Mn oxides (Bodeï et al., 2007; Cui et al., 2008; Feng et al., 2004; Golden et al., 1987). And more recently, a study by Feng et al. (2010) observed a topotactic transformation of layered biogenic Mn oxide minerals (δ-MnO_2) produced by *Pseudomonas putida* strain GB-1 to a nanoparticulate, poorly-crystalline todorokite phase through refluxing. This transformation resulted in todorokite phases comprised of thin layers containing a high degree of defects – tunnels strayed from 3×3 sizes (Feng et al., 2010) – likely similar in structure to todorokite phases produced by *A. strictum* in this study.

It has been established that solution chemistry (e.g., cation concentration, pH, and eH) can significantly impact the initial formation and subsequent transformation of both abiotic and biogenic minerals, particularly Mn oxides. Cations with a high enthalpy of hydration (e.g., Ca^{2+}, Mg^{2+}, Zn^{2+}, and Fe^{3+}) are typically required for the transformation of a hexagonal birnessite or δ-MnO_2-like phase (Bodeï et al., 2007; Feng et al., 2010). For example, several studies have demonstrated that Mn(II) oxidation products formed by spores of *Bacillus* sp. SG-1 transformed from an initial δ-MnO_2-like phase to a triclinic birnessite structure in a Ca-rich or seawater solution (Webb et al., 2005a,b) or to feitknechtite when exposed to high (1 mM) Mn concentrations (Bargar et al., 2005) within hours of exposure. Also, refluxing with high concentrations of Mg^{2+} promoted the transformation of the biogenic Mn oxide to a 10 Å triclinic phyllomanganate, which is the intermediate step in todorokite formation (Feng et al., 2010). If a similar process is operative for the fungi studied here, it is unclear as to what factors, in terms of solution chemistry, are initiating the transformation of the highly disordered, layered Mn oxides to a tunnel-type structure. The todorokite-like phase was deposited by only one fungal species and only when grown on a solid substrate, even though the 3 other species used in this study were grown under identical conditions (media composition, pH, $[Mn^{2+}]$). We predict that the metabolic activity or biochemistry of *A. strictum* strain DS1bioAY4a is altered during surface-attached growth. This altered activity either changes the local chemical environment or the mechanisms of Mn(II) oxidation employed by

A. strictum and is unlike those employed by the other fungal species studied here.

4. SUMMARY AND CONCLUSIONS

The results presented here demonstrate that the phylogeny and lifestyle (growth versus surface attached) of Mn(II)-oxidizing microorganisms are important factors in the resulting Mn oxide products. Although a poorly-ordered, nanocrystalline phyllomanganate similar to δ-MnO_2 is the initial oxide phase deposited by four different species of fungi, structural and morphological differences of these oxides and the secondary products (e.g., triclinic birnessite and todorokite) is largely species dependent – solution chemistry and growth conditions are the same for all species here. Furthermore, the same organism (*Acremonium* sp.) grown within the same media produces different Mn oxides when grown planktonically (δ-MnO_2) versus surface attached (δ-MnO_2 and todorokite). Due to the high reactivity of nanoparticulate oxides (Hochella et al., 2008), even minor morphological (including surface area, size, and porosity) and structural differences (layer vs. tunnel-structures) of the fungal biooxides could translate to large influences on biogeochemical processes in the environment (Cutting et al., 2009; Madden et al., 2005).

Differences in the morphology and depositional patterns among the fungal species suggest that more than one oxidation pathway is operative. For instance, the role of fungal enzymes (e.g., hyphae associated oxides on *P. cucumerina*), soluble extracellular polymers (e.g., templated oxides for *Stagonospora* sp.), and reactive oxygen species produced during cell differentiation (e.g., oxide formation at the base of fruiting bodies for *Pyrenochaeta* sp.) may all contribute to the oxidation of Mn(II) and the observed differences in the structure, morphology, and conversion of the Mn oxide products. Furthermore, the role of fungal organic templates in organizing Mn oxide structures and shifting thermodynamic barriers for precipitation of more crystalline phases warrants further investigation.

REFERENCES

Adams L. and Ghiorse W. (1987) Characterization of extracellular Mn super (2+)-oxidizing activity and isolation of an Mn super (2+)-oxidizing protein from *Leptothrix discophora* SS-1. *J. Bacteriol.* **169**, 1279–1285.

Aguirre J., Rìos-Momberg M., Hewitt D. and Hansberg W. (2005) Reactive oxygen species and development in microbial eukaryotes. *Trends Microbiol.* **13**, 111–118.

Bargar J. R., Fuller C. C., Marcus M. A., Brearley A. J., De Perez., la Rosa M., Webb S. M. and Caldwell W. A. (2009) Structural characterization of terrestrial microbial Mn oxides from Pinal Creek, AZ. *Geochim. Cosmochim. Acta* **73**, 889–910.

Bargar J. R., Tebo B. M., Bergmann U., Webb S. M., Glatzel P., Chiu V. Q. and Villalobos M. (2005) Biotic and abiotic products of Mn(II) oxidation by spores of the marine *Bacillus* sp. strain SG-1. *Am. Mineral.* **90**, 143–154.

Bent K. J. and Morton A. G. (1963) Formation and nature of swollen hyphae in *Penicillium* and related fungi. *Trans. Br. Mycol. Soc.* **46**, 401–408.

Bodeï S., Manceau A., Geoffroy N., Baronnet A. and Buatier M. (2007) Formation of todorokite from vernadite in Ni-rich hemipelagic sediments. *Geochim. Cosmochim. Acta* **71**, 5698–5716.

Boonfueng T., Axe L., Yee N., Hahn D. and Ndiba P. K. (2009) Zn sorption mechanisms onto sheathed *Leptothrix discophora* and the impact of the nanoparticulate biogenic Mn oxide coating. *J. Colloid Interface Sci.* **333**, 439–447.

Cahyani V., Murase J., Ishibashi E., Asakawa S. and Kimura M. (2009) Phylogenetic positions of Mn^{2+}-oxidizing bacteria and fungi isolated from Mn nodules in rice field subsoils. *Biol. Fertil. Soils* **45**, 337–346.

Chan C. S., De Stasio G., Welch S. A., Girasole M., Frazer B. H., Nesterova M. V., Fakra S. and Banfield J. F. (2004) Microbial polysaccharides template assembly of nanocrystal fibers. *Science* **303**, 1656–1658.

Chan C. S., Fakra S. C., Edwards D. C., Emerson D. and Banfield J. F. (2009) Iron oxyhydroxide mineralization on microbial extracellular polysaccharides. *Geochim. Cosmochim. Acta* **73**, 3807–3818.

Cui H., Liu X., Tan W., Feng X., Liu F. and Ruan H. D. (2008) Influence of Mn(III) availability on the phase transformation from layered buserite to tunnel-structured todorokite. *Clays Clay Miner.* **56**, 397–403.

Cutting R., Coker V., Fellowes J., Lloyd J. and Vaughan D. (2009) Mineralogical and morphological constraints on the reduction of Fe (III) minerals by *Geobacter sulfurreducens*. *Geochim. Cosmochim. Acta* **73**, 4004–4022.

de la Torre M. A. and Gomez-Alarcon G. (1994) Manganese and iron oxidation by fungi isolated from building stone. *Microbiol. Ecol.* **27**, 177–188.

Dick G. J., Lee Y. E. and Tebo B. M. (2006) Manganese(II)-oxidizing *Bacillus* spores in Guaymas Basin hydrothermal sediments and plumes. *Appl. Environ. Microbiol.* **72**, 3184–3190.

Emerson D., Garen R. and Ghiorse W. (1989) Formation of Metallogenium-like structures by a manganese-oxidising fungus. *Arch. Microbiol.* **151**, 223–231.

Fendorf S. E. and Zasoski R. J. (1992) Chromium(III) oxidation by δ-MnO_2. 1. characterization. *Environ. Sci. Technol.* **26**, 79–85.

Feng X., Tan W., Liu F., Wang J. and Ruans H. (2004) Synthesis of todorokite at atmospheric pressure. *Chem. Mater.* **16**, 4330–4336.

Feng X., Zhu M., Ginder-Vogel M., Ni C., Parikh S. and Sparks D. (2010) Formation of nano-crystalline todorokite from biogenic Mn oxides. *Geochim. Cosmochim. Acta* **1974**, 3232–3245.

Forrez I., Carballa M., Verbeken K., Vanhaecke L., SchluÄàsener M., Ternes T., Boon N. and Verstraete W. (2010) Diclofenac oxidation by biogenic manganese oxides. *Environ. Sci. Technol.* **44**, 3449–3454.

Francis C. A. and Tebo B. (2002) Enzymatic manganese(II) oxidation by metabolically dormant spores of diverse *Bacillus* species. *Appl. Environ. Microbiol.* **68**, 874–880.

Gadd G. M. (2007) Geomycology: biogeochemical transformations of rocks, minerals, metals and radionuclides by fungi, bioweathering and bioremediation. *Mycol. Res.* **111**, 3–49.

Ghiorse W. C. (1984) Biology of iron- and manganese-depositing bacteria. *Ann. Rev. Microbiol.* **38**, 515–550.

Golden D., Chen C. and Dixon J. (1987) Transformation of birnessite to buserite, todorokite, and manganite under mild hydrothermal treatment. *Clay Clay Mineral.* **35**, 271.

Grangeon S., Lanson B., Miyata N., Tani Y. and Manceau A. (2010) Structure of nanocrystalline phyllomanganates produced by freshwater fungi. *Am. Mineral.* **95**, 1608–1611.

Hansel C. M. and Francis C. A. (2006) Coupled photochemical and enzymatic Mn(II) oxidation pathways of a planktonic *Roseobacter*-like bacterium. *Appl. Environ. Microbiol.* **72**, 3543–3549.

Hochella, Jr., M., Lower S., Maurice P., Penn R., Sahai N., Sparks D. and Twining B. (2008) Nanominerals, mineral nanoparticles, and earth systems. *Science* **319**, 1631.

Hudson E. A., Allen P. G., Terminello L. J., Denecke M. A. and Reich T. (1996) Polarized x-ray absorption spectroscopy of the uranyl ion: comparison of experiment and theory. *Phys. Rev. B* **54**, 156–165.

Jurgensen A., Widmeyer J. R., Gordon R. A., Bendell-Young L. I., Moore M. M. and Crozier E. D. (2004) The structure of the manganese oxide on the sheath of the bacterium *Leptothrix discophora*: an XAFS study. *Am. Mineral.* **89**, 1110–1118.

Kay J., Conklin M., Fuller C. and O'Day P. (2001) Processes of nickel and cobalt uptake by a manganese oxide forming sediment in Pinal Creek, globe mining district, Arizona. *Environ. Sci. Technol.* **35**, 4719–4725.

Krumbein W. E. and Jens K. (1981) Biogenic rock varnishes of the Negev Desert (Israel): an ecological study of iron and manganese transformation by cyanobacteria and fungi. *Oecologia* **50**, 25–38.

Lanson B., Drits V., Feng Q. and Manceau A. (2002) Structure of synthetic Na-birnessite: evidence for a triclinic one-layer unit cell. *Am. Mineral.* **87**, 1662.

Lanson B., Drits V., Silvester E. and Manceau A. (2000) Structure of H-exchanged hexagonal birnessite and its mechanism of formation from Na-rich monoclinic buserite at low pH. *Am. Mineral.* **85**, 826.

Learman D. R., Voelker B. M., Vazquez-Rodriguez A. I. and Hansel C. M. (2011) Formation of manganese oxides by bacterially generated superoxide. *Nature Geo.* **4**, 95–98.

Madden A. S. and Hochella, Jr., M. F. (2005) A test of geochemical reactivity as a function of mineral size: manganese oxidation promoted by hematite nanoparticles. *Geochim. Cosmochim. Acta* **69**, 389–398.

Malinowski E. R. (1978) Theory of error for target factor analysis with applications to mass spectrometry and nuclear magnetic resonance spectrometry. *Anal. Chim. Acta* **103**, 359–364.

Manceau A., Marcus M. A. and Tamura N. (2002) Quantitative speciation of heavy metals in soils and sediments by synchrotron X-ray techniques. In *Applications of synchrotron radiation in low-temperature geochemistry and environmental science* (eds. P. A. Fenter, M. L. Rivers, N. C. Sturchio and S. R. Sutton). Mineralogical Society of America, Washington, DC.

Mandernack K. W., Post J. and Tebo B. M. (1995) Manganese mineral formation by bacterial spores of the marine Bacillus, strain SG-1: evidence for the direct oxidation of Mn(II) to Mn(IV). *Geochim. Cosmochim. Acta* **59**, 4393–4408.

Marcus M. A., Manceau A. and Kersten M. (2004) Mn, Fe, Zn, and As speciation in a fast-growing ferromanganese marine nodule. *Geochim. Cosmochim. Acta* **68**, 3125–3136.

Mariner R., Johnson D. and Hallberg K. (2008) Characterisation of an attenuation system for the remediation of Mn (II) contaminated waters. *Hydrometallurgy* **94**, 100–104.

Matocha C. J., Elzinga E. J. and Sparks D. L. (2001) Reactivity of Pb(II) at the Mn(III, IV) (Oxyhydr)oxide–water interface. *Environ. Sci. Technol.* **35**, 2967–2972.

McKeown D. A. and Post J. E. (2001) Characterization of manganese oxide mineralogy in rock varnish and dendrites using X-ray absorption spectroscopy. *Am. Mineral.* **86**, 701–713.

Miyata N., Maruo K., Tani Y., Tsuno H., Seyama H., Soma M. and Iwahori K. (2006a) Production of biogenic manganese oxides by anamorphic Ascomycete fungi isolated from stream-bed pebbles. *Geomicrobiol. J.* **23**, 63–73.

Miyata N., Tani Y., Iwahori K. and Soma M. (2004) Enzymatic formation of manganese oxides by an *Acremonium*-like hyphomycete fungus, strain KR 21–2. *FEMS Microbiol. Ecol.* **47**, 101–109.

Miyata N., Tani Y., Maruo K., Tsuno H., Sakata M. and Iwahori K. (2006b) Manganese(IV) oxide production by Acremonium sp. strain KR21–2 and extracellular Mn(II) oxidase activity. *Appl. Environ. Microbiol.* **72**, 6467–6473.

Murray K., Mozafarzadeh M. and Tebo B. (2005) Cr (III) oxidation and Cr toxicity in cultures of the manganese (II)-oxidizing *Pseudomonas putida* strain GB-1. *Geomicrobiol. J.* **22**, 151–159.

Murray K. and Tebo B. (2007) Cr (III) is indirectly oxidized by the Mn (II)-oxidizing bacterium *Bacillus* sp. strain SG-1. *Environ. Sci. Technol.* **41**, 528–533.

Nealson K., Tebo B. and Rosson R. (1988) Occurrence and mechanisms of microbial oxidation of manganese. *Adv. Appl. Microbiol.* **33**, 279–318.

Nelson Y. M., Lion L. W., Ghiorse W. C. and Shuler M. L. (1999) Production of biogenic Mn oxides by *Leptothrix descophora* SS-1 in a chemically defined growth medium and evaluation of their Pb adsorption characteristics. *Appl. Environ. Microbiol.* **65**, 175–180.

Newville M. (2001) IFEFFIT: interactive XAFS analysis and FEFF fitting. *J. Synch. Rad.* **8**, 324–332.

O'Reilly S. and Hochella M. (2003) Lead sorption efficiencies of natural and synthetic Mn and Fe-oxides. *Geochim. Cosmochim. Acta* **67**, 4471–4487.

Peña J., Kwon K. D., Refson K., Bargar J. R. and Sposito G. (2010) Mechanisms of nickel sorption by a bacteriogenic birnessite. *Geochim. Cosmochim. Acta* **74**, 3076–3089.

Petkov V., Ren Y., Saratovsky I., PasteÃÅn P., Gurr S. J., Hayward M. A., Poeppelmeier K. R. and Gaillard J.-F. (2009) Atomic-scale structure of biogenic materials by total x-ray diffraction: a study of bacterial and fungal MnOx. *ACS Nano* **3**, 441–445.

Post J. E. (1998) Manganese oxide minerals: crystal structures and economic and environmental significance. *Proc. Natl. Acad. Sci. USA* **96**, 3447–3454.

Ressler T., Brock S. L., Wong J. and Suib S. L. (1999) Multiple scattering EXAFS analysis of tetraalkylammonium manganese oxide colloids. *J. Phys. Chem. B* **103**, 6407–6420.

Santelli C. M., Pfister D., Lazarus D., Sun L., Burgos W. D. and Hansel C. M. (2010) Diverse fungal and bacterial communities promote Mn(II)-oxidation and remediation of coal mine drainage in passive treatment systems. *Appl. Environ. Microbiol.* **76**, 4871–4875.

Saratovsky I., Gurr S. and Hayward M. (2009) The structure of manganese oxide formed by the fungus *Acremonium* sp. strain KR21–2. *Geochim. Cosmochim. Acta* **73**, 3291–3300.

Silvester E., Manceau M. and Drits V. (1997) Structure of synthetic monoclinic Na-rich birnessite and hexagonal birnessite: II. Results from chemical studies and EXAFS spectroscopy. *Am. Mineral.* **82**, 962–978.

Sunda W. and Huntsman S. (1994) Photoreduction of manganese oxides in seawater. *Mar. Chem.* **46**, 133–152.

Sunda W. and Kieber D. (1994) Oxidation of humic substances by manganese oxides yields low-molecular-weight organic substrates. *Nature* **367**, 62–64.

Takahashi Y., Manceau A., Geoffroy N., Marcus M. and Usui A. (2007) Chemical and structural control of the partitioning of Co, Ce, and Pb in marine ferromanganese oxides. *Geochim. Cosmochim. Acta* **71**, 984–1008.

Tebo B., Ghiorse W., van Waasbergen L., Siering P. and Caspi R. (1997) Bacterially mediated mineral formation; insights into manganese (II) oxidation from molecular genetic and biochemical studies. In *Geomicrobiology: interactions between microbes and minerals* (eds. J. F. Banfield and K. H. Nealson). Mineralogical Society of America, Washington, DC.

Templeton A. S., Staudigel H. and Tebo B. M. (2005) Diverse Mn(II)-oxidizing bacteria isolated from submarine basalts at Loihi Seamount. *Geomicrobiol. J.* **22**, 127–139.

Thompson I., Huber D., Guest C. and Schulze D. (2005) Fungal manganese oxidation in a reduced soil. *Environ. Microbiol.* **7**, 1480–1487.

Toner B., Fakra S., Villalobos M., Warwick T. and Sposito G. (2005) Spatially resolved characterization of biogenic manganese oxide production within a bacterial biofilm. *Appl. Environ. Microbiol.* **71**, 1300–1310.

Toner B., Manceau A., Webb S. M. and Sposito G. (2006) Zinc sorption to biogenic hexagonal-birnessite particles within a hydrated bacterial biofilm. *Geochim. Cosmochim. Acta* **70**, 27–43.

Villalobos M., Bargar J. and Sposito G. (2005) Mechanisms of Pb (II) sorption on a biogenic manganese oxide. *Environ. Sci. Technol.* **39**, 569–576.

Villalobos M., Lanson B., Manceau A., Toner B. and Sposito G. (2006) Structural model for the biogenic Mn oxide produced by *Pseuomonas putida*. *Am. Mineral.* **91**, 489–502.

Villalobos M., Toner B., Bargar J. and Sposito G. (2003) Characterization of the manganese oxide produced by *Pseudomonas putida* strain MnB1. *Geochim. Cosmochim. Acta* **67**, 2649–2662.

Webb S. M. (2005) SIXPACK: a graphical user interface for XAS analysis using IFEFFIT. *Phys. Scripta.* **T115**, 1011–1014.

Webb S. M., Fuller C. C., Tebo B. M. and Bargar J. R. (2006) Determination of uranyl incorporation into biogenic manganese oxides using X-ray absorption spectroscopy and scattering. *Environ. Sci. Technol.* **40**, 771–777.

Webb S. M., Tebo B. M. and Bargar J. R. (2005a) Structural characterization of biogenic Mn oxides produced in seawater by the marine *Bacillus* sp. strain SG-1. *Am. Mineral.* **90**, 1342–1357.

Webb S. M., Tebo B. M. and Bargar J. R. (2005b) Structural influences of sodium and calcium ions on the biogenic manganese oxides produced by the marine *Bacillus* sp., strain SG-1. *Geomicrobiol. J.* **22**, 181–193.

Zhu M., Ginder-Vogel M., Parikh S. J., Feng X.-H. and Sparks D. L. (2010) Cation Effects on the Layer Structure of Biogenic Mn–Oxides. *Environ. Sci. Technol.* **44**, 4465–4471.